Simulation of fluid flow and collection efficiency for an SEA multi-element probe

David L. Rigby[1]
Vantage Partners Limited, Cleveland, OH, 44135

Peter M. Struk[2]
NASA Glenn Research Center, Cleveland, OH, 44135

and

Colin Bidwell[3]
NASA Glenn Research Center, Cleveland, OH, 44135

Numerical simulations of fluid flow and collection efficiency for a Science Engineering Associates (SEA) multi-element probe are presented. Simulation of the flow field was produced using the Glenn-HT Navier-Stokes solver. Three-dimensional unsteady results were produced and then time averaged for the heat transfer and collection efficiency results. Three grid densities were investigated to enable an assessment of grid dependence. Simulations were completed for free stream velocities ranging from 85-135 m/s, and free stream total pressure of 44.8 and 93.1 kPa (6.5 and 13.5 psia). In addition, the effect of angle of attack and yaw were investigated by including 5 degree deviations from straight for one of the flow conditions. All but one of the cases simulated a probe in isolation (i.e. in a very large domain without any support strut). One case is included which represents a probe mounted on a support strut within a finite sized wind tunnel. Collection efficiencies were generated, using the LEWICE3D code, for four spherical particle sizes, 100, 50, 20, and 5 micron in diameter. It was observed that a reduction in velocity of about 20% occurred, for all cases, as the flow entered the shroud of the probe. The reduction in velocity within the shroud is not indicative of any error in the probe measurement accuracy. Heat transfer results are presented which agree quite well with a correlation for the circular cross section heated elements. Collection efficiency results indicate a reduction in collection efficiency as particle size is reduced. The reduction with particle size is expected, however, the results tended to be lower than the previous results generated for isolated two-dimensional elements. The deviation from the two-dimensional results is more pronounced for the smaller particles and is likely due to the reduced flow within the protective shroud. As particle size increases differences between the two-dimensional and three-dimensional results become negligible. Taken as a group, the total collection efficiency of the elements including the effects of the shroud has been shown to be in the range of 0.93 to 0.99 for particles above 20 um. The 3D model has improved the estimated collection efficiency for smaller particles where errors in previous estimates were more significant.

1. Introduction

The liquid and/or ice-water content in clouds is an important parameter in aircraft icing research. A common method to measure water content is through the use of hot-wires or heated elements inserted into a flow whether in a wind tunnel or mounted on a research aircraft. The impinging water droplets or ice particles strike the hot wire and evaporate. The power required to evaporate the water is measured and is then directly related to the amount of impinging water. One such probe is the SEA multi-element probe [1] which includes three heated elements of different geometries designed to discriminate between water droplet sizes including super-cooled large droplets (SLD). The center element of this probe uses a half-pipe geometry designed to catch and retain ice particles (which may bounce away on cylindrical elements) as well as the liquid

[1] Senior Research Engineer
[2] Aerospace Engineer, Icing Branch, 21000 Brookpark Road, AIAA Senior Member
[3] Aerospace Engineer, Icing Branch, 21000 Brookpark Road, AIAA Senior Member

droplets. Thus the center element is thought of as the total water sensing element. The half-pipe element also happens to retain super-cooled large droplets better than the cylindrical elements.

Due to engine-icing issues related to ingestion of ice crystals[2], a variant of the initial multi-element probe is now being used to measure water content in ice-crystal clouds [3-7]. Recent imaging of the probe in an ice-crystal cloud suggests that complete evaporation may not be occurring uniformly across the elements [7]. Figure 1 shows a sample image where roughly half of the center element appears to be wetted. Close examination of the images (see inset in figure 1) further suggests that water may be running out of this element and carried away downstream by the flow.

To better understand the behavior of this probe in ice-crystal conditions, NASA has undertaken two studies related to the multi-element probe. The first study, described in this paper, examines the flow around and through the multi-element probe via a detailed flow solution and particle trajectory study. The second study, presented in a complementary paper at this conference, examines the thermal behavior of the probe via a thermal analysis [8].

2. Description

A view of the SEA probe is shown in figure 2. On the left is a CAD image that includes the base and mounting strut. The three sensing elements are visible within the shroud. A fourth sensing element can be seen on the bottom of the shroud behind the three vertical elements. On the right is an image showing the surface grids from the numerical simulation. The shroud and three vertical sensing elements are accurately represented. The base, mounting strut, and fourth sensing element are omitted to simplify the analysis. Results with the strut omitted are desirable so that a comparison will be possible with results that include the strut. All but one of the cases presented in this paper represent an isolated probe with no supporting strut.

Figure 3 shows a schematic of the probe cross-section. The probe is positioned at the origin (figure 3) and has an inner diameter of 13.41 mm (0.5278 inches). The axis of the shroud is oriented in the x-direction and the three sensing elements are in the y-direction. Two round elements, a thick 2.1082 mm (0.083 inch) diameter one and a thin 0.5334 mm (0.021 inch) diameter one are located at x=0 and are offset in the z-direction by 5.08 mm (0.2 inches). The third element is a semi-circle, or half-pipe configuration, and is centered in the shroud in the z-direction, and located 3.81 mm (0.15 inches) downstream of the other two elements. The shroud extends to approximately 20 mm (0.795 inch) upstream and 37 mm (1.455 inches) downstream of the pair of round elements.

The computational domain is chosen in an effort to produce results for an isolated probe. The extent of the domain is ± 381 mm (15 inches) in each of the three Cartesian directions. The grid is a body fitted structured multi-block grid consisting of 767 blocks. Three grid densities were investigated with approximately 7 million, 3 million and 0.9 million cells, respectively. For each grid, the physical size and shape of each block was unchanged. Only the grid density within each block was modified.

Table 1 presents a summary of the cases. The conditions were chosen to match available experimental results. A companion paper, at this conference [8], uses the results of this study. Results are presented for free stream velocities of 86, 100, and 135 m/s. The set of three velocities are run at two different free stream total pressures of 44.8 and 93.1 kPa (6.5 and 13.5 psia). The air stream is cold (-5 C), the shroud is held at a warm temperature (50 C), and the heated sensing elements are hot (140 C). The first six cases in table 1 are run straight on (i.e. no angle of attack or yaw). The remaining five cases are all at the same free stream conditions of 85 m/s velocity and 93.1 kPa total pressure. A case is presented at 5 degree angle of attack, then one at 5 degrees yaw. A separate case is done which includes the support strut. The case with the strut is placed in the center of a wind tunnel that is 135.128 mm (5.32 inches) tall by 254 mm (10 inches) wide. The last two cases in table 1 correspond to coarsening and refining the grid used for all the other cases. The coarse grid is uniformly coarsened by a factor of 4:6. The finer grid is uniformly refined by a factor of 8:6.

3. Results

a. Overview

Flow solutions are produced using the Glenn-HT Navier-Stokes code [9]. For each of the cases, a time accurate URANS (unsteady Reynolds Averaged Navier-Stokes) solution is performed using a Wilcox k-omega turbulence model. The simulation is allowed to develop until the flow appears stationary (i.e. unsteady, but not drifting). Then a running average is performed to produce the time-averaged result. Figure 4 shows a representative snapshot showing the instantaneous (figure 4a) and time averaged (figure 4b) results. The quantity shown in figure 4 is the y-vorticity, which is the vorticity pointing into the page. The scale in both plots is the same. From figure 4a it is apparent that significant shedding is occurring downstream of the heated elements. Admittedly, the URANS approach will not capture the fine details of the unsteady flow,

but it was assumed that it would likely produce reasonable time averaged results even if the details of the unsteadiness were not perfectly captured. As will be shown below, heat transfer on the circular elements shows reasonable agreement with the correlation of Sparrow [10]. The time step used in the majority of the simulations was 1.73 microseconds. For the finer and coarser grids the time step was scaled by the same factor as the grid spacing. This choice of time step produces between 50 and 100 steps in each of the dominant cycles produced by the shedding from the heated elements. The time averaging is done over a period that includes approximately 100 shedding cycles.

These simulations were run in parallel on the NASA Advanced Supercomputing machine Pleiades. Each case required approximately 30 hours using 84 CPUs. The finer grid simulation required approximately three times as long to run, while the coarser grid required about one quarter the time.

Figure 5 shows the pressure distribution in and around the probe. In figure 5 the probe surfaces, as well as the symmetry plane are shown colored by static pressure (red is high and blue is low). Notice that the pressure in the region between the shroud inlet and the sensing elements is higher indicating a reduction in speed. Figure 6 shows the symmetry plane colored by axial velocity. In addition, white lines indicate the regions of reverse flow. Reverse flow regions are observed around the outside of the shroud near the inlet. Reverse flow regions also exist downstream of each of the sensing elements, as well as small regions at the trailing edge of the shroud.

To quantify the reduction in speed within the shroud, the average mass flux within the shroud divided by the free stream mass flux (which will be referred to as the Normalized Average Shroud Mass Flux) was calculated for each of the cases. Table 2 shows the Normalized Average Shroud Mass Flux for each case. It can be seen that the normalized mass flux is quite constant at about 80%. Figure 7 shows how the normalized mass flux varies as the grid is changed. The coarse grid allows about 3% more mass to pass, while the finer grid allows about 1% less compared to the baseline grid. It would appear that the results on the base grid are likely within 3% of the theoretical zero grid spacing result.

b. Heat Transfer Results

i. Global Average Results

It is desirable to have average heat transfer results over the entire heating element as well as only for the front facing surfaces. The frontal result is useful when considering the cases running with liquid water or ice content, since particles generally only hit the frontal area. Tables 3 and 4 present the front and overall average Nusselt numbers for the six straight on cases. The Reynolds numbers for the thick (083) and thin (021) wires are presented also. Note the half pipe (or scoop) is the same diameter as the thick wire and so has the same Reynolds number. All properties for the Reynolds and Nusselt numbers are evaluated at the film temperature. Where the film temperature is taken to be the simple average between the free stream total temperature and the surface temperature. Figure 8 shows the data from tables 3 and 4. In addition the correlation of Sparrow is plotted. Note that in the Sparrow correlation all quantities are evaluated at the free stream conditions, except for the viscosity at the surface. To plot the Sparrow correlation in figure 8 a simple substitution was made to account for film conditions versus free stream conditions. The original Sparrow correlations is stated as

$$Nu = 0.25 + \left[0.4Re^{\frac{1}{2}} + 0.06Re^{2/3}\right]\mathrm{Pr}^{0.37}\left[\frac{\mu}{\mu_s}\right]^{\frac{1}{4}} \tag{1}$$

The Reynolds number and Nusselt number, based on approach conditions, are

$$Re = \frac{(\rho U)_{sh} d_o}{\mu_{sh}} \tag{2}$$

$$\mathrm{Nu} = \mathrm{h} * \frac{d_0}{k_{sh}} \tag{3}$$

Where the subscript “sh” refers to inside the shroud upstream of the sensing elements. For the present work it is preferred to present results in terms of parameters evaluated at film temperature, so a simple conversion is used. Given Reynolds number and Nusselt number, defined above, the film version of these are simply

$$Re_{film} = \frac{\rho_{\text{film}} U_{\text{sh}} d_{\text{o}}}{\mu_{\text{film}}} = \left(\frac{\mu_{\text{film}}}{\mu_{\text{sh}}}\right)\left(\frac{\rho_{\text{sh}}}{\rho_{\text{film}}}\right) Re \quad (4)$$

$$Nu_{film} = h * \frac{d_0}{k_{film}} = \left(\frac{k_{sh}}{k_{film}}\right) Nu \quad (5)$$

As can be seen in figure 8, the agreement for the circular heated elements is quite good when compared to the Sparrow correlation. The front part of the circular elements always produces a higher average, as expected. The overall Nusselt number on the half-pipe is always lower than the circular element. In contrast to the circular elements, it is noted that the frontal Nusselt number is lower than the overall on the half-pipe. This result is not unexpected, as there is a large stagnant region upstream of the half-pipe. Figure 9 shows the results from the coarsened and refined grids compared to the base (fine) grid. For the most part the results do not seem to vary much, especially between the fine and finer grids. However, the Scoop_Overall result did not seem to flatten out, like the other values. It would appear that the Scoop_Overall result might need additional grid refinement if a tighter estimate is required.

ii. Spanwise Distributions

Figure 10 presents the spanwise distribution of the heat transfer results. For each heated element a front average and an overall average is presented as a function of spanwise location. In each plot there are six solid lines corresponding to the six straight on cases (i.e. probe aligned with the flow). Two additional dashed lines show the coarser and finer result for the Pt13p5V085 case. Generally the base grid and finer grid show good agreement. The coarser grid agrees well on the Thin element, but deviates substantially on the Thick and Scoop heated elements.

Figure 11 shows normalized average Nusselt number results. These curves were generated by first normalizing each curve in figure 10 by it own average value and then averaging the result from the six straight on cases. The intent is to generate a representative spanwise distribution for each element. Generally the front averages (the right column) show less spanwise variation. The overall average results (the left column) are fairly flat for the Thin element, while the Thick and Scoop elements show gradually increasing values as the shroud is approached followed by a drop off closer to the shroud. The Scoop also has a sharp increase very near the shroud.

iii. Other Cases

Tables 5 and 6 contain the average Nusselt number results for the cases run to test the effect of off axis flow. The results of the case Pt13p5V085 are repeated for comparison. Slight variations in the Reynolds numbers are due to small changes in the mass flow through the shroud. It can be seen that most of the Nusselt number averages are very close between the four cases in table 5 and 6. The notable exception is for the result with the support in place, the Scoop Overall value is 3% lower and the Scoop front result is 1% lower. Putting the probe at an angle of attack or in yaw had very little effect on the results. Figure 12 shows the spanwise results for the non-axisymmetric cases. The scale is chosen to match that of figure 10 so that it can quickly be appreciated that very little changes occur in comparison to the changes resulting from the other flow conditions. It is difficult to see any deviation, except for the With Support case on the Scoop (the bottom two plots)

c. Collection Efficiency Results

i. Introduction

Collection efficiency is calculated on all of the surfaces using the LEWICE3D code [13]. The LEWICE3D code uses the provided flow solution to predict particle trajectories and impingement. Results are generated for four particle sizes, 100, 50, 20, and 5 micron in diameter. In addition, for the 100 micron particle size a super-cooled large droplet (SLD) analysis is done which takes into account possible splashing. Local collection efficiency, β, is defined as the ratio of the surface mass flux of particles to the free stream mass flux of particles. A local collection efficiency of one implies the surface flux rate of particles is equal to the free stream flux rate of particles. Local collection efficiency is dependent upon the amount of convergence or dispersion of particles in a flow and the orientation of the surface relative to the droplet paths. It is important to appreciate the effect of surface orientation on the local collection efficiency. A surface which is oriented at any angle other than perpendicular to the main flow direction would be expected to produce a local collection efficiency below unity even if it collects all of the particles from its projected area.

For particles of a given size, the particle with a smaller mass will adapt to the flow more quickly than a particle with a larger mass. The more massive particles, which are more resistant to changes in velocity, are less apt to avoid obstacles in their path and hence generate higher collection efficiencies. Several non-dimensional parameters have been developed over the years to characterize the combined effect of flow, drag and particle inertia on the collection efficiency for a geometry. These include the inertia parameter, K, and the Bragg modified inertia parameter, K_0 [11]. The inertia parameter which increases with drop size and speed is a non-dimensional measure of the relaxation time of a particle. That is the time it takes a particle velocity to relax to the flow velocity. The inertia parameter characterizes the effect of particle mass, geometry scale and flow viscosity but it does not incorporate the effect of the particle Reynolds number. The Bragg modified inertia parameter incorporates the effect of particle Reynolds number. For a given geometry, a particle flow with the same Bragg modified inertia parameter will generate the same particle trajectory scaling and hence the same collection efficiency.

Here, the definition of K_0 follows that derived by Bragg [11]. The value of K_0 varies based on the particle size and type, hot-wire size, and freestream velocity as captured by the Reynolds number, Re_δ, and the original inertia parameter, K, as shown in Eq. (7) and Eq. (8), respectively. In Eq. (7), the air properties are evaluated using the freestream (i.e. not shroud) conditions. In Eq.(8), the density, ρ, corresponds to either liquid water or ice.

$$K_0 = 18K\left[Re_\delta^{-2/3} - \sqrt{6}Re_\delta^{-1}\tan^{-1}\left(\frac{Re_\delta^{1/3}}{\sqrt{6}}\right)\right] \tag{6}$$

$$Re_\delta = \frac{\rho_{a,\infty}U_\infty\delta}{\mu_{a,\infty}} \tag{7}$$

$$K = \frac{\rho\delta^2 U_\infty}{18d_o\mu_{a,\infty}} \tag{8}$$

Total collection efficiency, E_m, is the ratio of the particle mass impinging on a body to the free stream impingement rate through an area equal to the projected area of the body. Calculations were made using LEWICE [12] for isolated 2D wire models and using a LEWICE3D [13] wire centerline analysis of the 3 SEA probe wires. LEWICE is a 2D, multi-time step ice accretion code. A total collection efficiency of one, which is large, indicates that the impacting particles trajectories are straight which implies a large modified inertia parameter.

ii. Discussion of Collection Efficiency Results

The results for total collection efficiency, E_m, for the 3 wires are shown in table 7. Calculations were made using LEWICE [12] for isolated 2D wire models and using a LEWICE3D [13] wire centerline analysis of the 3 SEA probe wires. Table 7 shows the various particle parameters calculated for the SEA probe analysis. The table shows the increase in the modified inertia parameters with particle size for the straight on cases. From the table we can also see that the higher speed straight on case has a larger modified inertia parameter than the lower speed cases. The increase in modified inertia parameter over the low speed cases results in an increase in total collection efficiency, E_m, for the wires and shroud, which can be seen in the final column of table 7. From the table we can also see that the change in total collection efficiency is very small between the 50 μm and the 100 μm cases. As the modified inertia parameter increases the collection efficiency converges to a maximum value. This is because the particle momentum has increased to a point where it is much larger than the drag force generated by the geometry based flow disturbance. At this point the drag forces can be neglected and the particle paths are straight lines. Increasing the particle size in this regime does very little to change the collection efficiency because the particle paths are all relatively straight. The data from table 7 was plotted and fit to curves presented elsewhere in this conference [8].

The total collection increased with increased inertia parameter for all 3 three wires for the 2D and 3D analysis. The 3D results showed reduced values of total collection efficiency compared to the 2D results for the same conditions. This was especially evident for the smaller modified inertia parameter cases (19% smaller, when comparing the 3D to 2D result, for the 5 μm, 85 m/s, 6.5 psia, large cylinder case). Lower total collection efficiency from the 3D analysis can be attributed to the effect of the shroud. Two factors can be identified. The first factor is the fact that the normalized mass flux within the shroud is approximately 80%. This reduced mass flux would cause a reduction in the flux of particles entering the shroud. The second factor would be the fact that the velocity within the shroud is smaller than in the freestream, which makes it easier for a particle to avoid an obstacle. As the particles size increases, the effect of the shroud becomes negligible.

Figure 13 summarizes the local collection efficiency results for the straight on cases. We can see that the collection efficiency increases with particle size for all three wires and the probe shroud. This is due to the increased inertia of the larger

particles. It can also be seen that there is very little variation across the span of each heated element. The total collection efficiency result from table 7 is included for each case to provide quantitative comparison.

The results for the other (i.e. pitch, yaw, and with support strut) flow cases are shown in figure 14. The results follow the same trend for the straight on cases in that increasing the modified inertia parameter results in an increase in collection efficiency for all three wires and the shroud. For the cases without the strut we can see from the figure that size of the shadow zone (zero local collection efficiency regions at ends of wire) increases with particle size. This is because the smaller particles more easily follow the flow around the shroud lip than the larger particles. For the strut cases the shadow zone size increases with decreased particle size. For smaller particles the strut generates a flow disturbance ahead of the shroud that, in some ways, is similar to increasing the local yaw angle. The small particles react to this disturbance more readily than the larger particles due to their increased inertia resulting in a larger shadow zone.

The super-cooled large droplet (SLD) splashing results for the straight on cases are shown in fig. 15. We can see that there is very little difference in the collection efficiency distribution for the 100 μm non-splashing cases. The small difference results because the modified inertia parameter for all three cases are relatively large implying the collection efficiency has converged to its maximum value. The splashing results show the subtle effect of the SLD splashing model. The collection efficiencies are slightly reduced at the impingement limits on the wires and shroud for the splashing cases because this is where the SLD model generates the maximum mass loss. Re-impingement on the wires from the shroud impacts can be seen as concentric rings of increased collection efficiency on the 3 wires. The half-pipe wire shows an increase in collection efficiency with increased modified inertia parameter. This is due to an increase in re-impingement on this element from the particles splashed from the other wires and the shroud. It is also due to splashing from the sidewalls of the half-pipe element itself, which tends to concentrate the mass more towards the center of the element. As the inertia parameter is increased the amount of mass ejected from a droplet impact increases resulting in more mass re-impingement in other regions.

Figure 16 shows the splashing results for the other cases. The results are similar for the straight on cases. There is evidence of lower mass near the impingement limits for the splashing cases and the splashing from the shroud generates concentric rings of increased impingement on the wires. The half-pipe wire splashing cases also show increased levels of impingement due to re-impingement from the elements sidewalls and the other elements. The size of the shadow zone does not appear to be affected by splashing. This is because the shadow zone limit is controlled by the particles that graze the shroud lip and these particles are not affected by splashing.

4. Conclusion

Numerical simulations of flow and collection efficiency have been presented for an SEA multi-element probe. The results provide insight into the effect of the shroud and the neighboring sensing elements. The flow velocity just upstream of the sensing elements is observed to be approximately 20% lower than the free stream value for all cases considered. The reduction in velocity within the shroud is not indicative of any error in the probe measurement accuracy.

Global averages for the Nusselt number were produced for each of the three sensing elements. Nusselt number results were separated into frontal and overall results, since the frontal results can facilitate analysis of wet conditions. The overall averages for the circular cross section elements agree reasonably with an available empirical correlation. Spanwise distributions of Nusselt number were also produced. Generally the frontal values show less variation along the span than the overall values.

Collection efficiency results exhibit the expected trend of reducing as particles size becomes small. Collection efficiency results showed minimal spanwise variation for straight-on cases for all particle sizes examined. However, the present 3D total collection efficiencies are generally below previous results from two-dimensional, isolated element results. The deviation between 3D and 2D results becomes more pronounced as the particle size is reduced and becomes negligible as the particle size increases. Taken as a group, the total collection efficiency of the elements including the effects of the shroud has been shown to be in the range of 0.93 to 0.99 for particles above 20 um. The 3D model has improved the estimated collection efficiency for smaller particles where errors in previous estimates were more significant.

5. Acknowledgments

This work is supported by the Atmospheric Environment Safety Technology Project (AEST) in the NASA Aviation Safety Program, and is part of the Engine Icing Technical Challenge. The authors wish to acknowledge Lyle Lilie and the staff of Science Engineering Associates for information regarding the Multi-Wire probe as well as guidance on the interpretation of results.

Nomenclature

CFD = computational fluid dynamics
d = diameter
E_m = Total Collection Efficiency
IWC = Ice Water Content
K = Inertia parameter (equation 8)
K_0 = Bragg modified inertia parameter (equation 6)
LWC = liquid water content (g / m^3)
MVD = median volumetric diameter
Nu = Nusselt number
P = static pressure (kPa)
Pr = Prandtl number
R = Radius
Re = Reynolds number
SLD = super-cooled large droplet
T = static air temperature (°C)
T_b = boundary temperature (°C)
U = freesteam velocity (m/s)
X = Cartesian direction aligned with probe shroud axis
Y = Cartesian direction aligned with heated element axes
Z = Cartesian direction perpendicular to X and Y

Greek Symbols

α = Angle of attack (rotation about the Y-axis)
β = Local Collection Efficiency
γ = Yaw angle (rotation about the Z-axis)
δ = Particle mean volumetric diameter (MVD) for water or mean mass diameter (MMD) for ice
μ = dynamic viscosity
ρ = mass density (kg / m^3)

Subscripts

a = air
$film$ = film (for temperature); $T_f = (T_s + T_0)/2$
HP = reference to half-pipe hot-wire element
sh = shroud conditions
thin = refers to 021 heated element
thick = refers to 083 heated element
∞ = ambient or upstream conditions in the tunnel
0 = total conditions
021 = reference to smaller LWC hot-wire element
083 = reference to larger LWC hot-wire element
2D = result from two dimensional isolated cylinder
3D = result from center of three dimensional analysis

References

[1]**Lilie, L., Emery, E., Strapp, J. W., and Emery, J. "A Multiwire Hot-Wire Device for Measurement of Icing Severity, Total Water Content, Liquid Water Content, and Droplet Diameter " *43rd AIAA Aerospace Sciences Meeting and Exhibit*, AIAA-2005-859, 2005.**

[2]**Mason, J. G., Strapp, J. W., and Chow, P. "The Ice Particle Threat to Engines in Flight," *44th AIAA Aerospace Sciences Meeting and Exhibit*, AIAA-2006-206, 2006.**

[3]**Mason, J. G., Chow, P., and Fuleki, D. M. "Understanding Ice Crystal Accretion and Shedding Phenomenon in Jet Engines using a Rig Test," *ASME Turbo Expo 2010*, GT2010-22550, 2010.**

[4]**Fuleki, D. M., and MacLeod, J. D. "Ice Crystal Accretion Test Rig Development For A Compressor Transition Duct," *AIAA Guidance, Navigation, and Control Conference*, AIAA 2010-7529, 2010.**

[5]**Knezevici, D. C., Fuleki, D., and MacLeod, J. "Development and Commissioning of the Linear Compressor Cascade Rig for Ice Crystal Research," *International Conference on Aircraft and Engine Icing and Ground Deicing*, 2011-38-0079, 2011.**

[6]**Struk, P., Currie, T., Wright, W. B., Knezevici, D. C., Fuleki, D., Broeren, A., Vargas, M., and Tsao, J. "Fundamental Ice Crystal Accretion Physics Studies," *SAE 2011 International Conference on Aircraft and Engine Icing and Ground Deicing*, 2011-38-0018 or NASA/TM-2012-217429, 2011.**

[7]**Struk, P. M., Bencic, T., Tsao, J., Fuleki, D., and Knezevici, D. C. "Preparation for Scaling Studies of Ice-Crystal Icing at the NRC Research Altitude Test Facility," *5th AIAA Atmospheric and Space Environments Conference*, AIAA-2013-2675 and NASA/TM-2013-216571, 2013.**

[8]**Struk, P. M., Rigby, D. L. and Venkataraman, K. "A Thermal Analysis of a Hot-Wire Probe for Icing Applications," *6th Atmospheric and Space Environments Conference*, American Institute of Aeronautics and Astronautics, Atlanta, GA (submitted for publication).**

[9]**Steinthorsson, E.; Liou, M.S.; and Povinelli, L.A.: Development of an Explicit Multiblock/Multigrid Flow Solver for Viscous Flows in Complex Geometries. AIAA–93–2380 (NASA TM–106356), 1993.**

[10]**Sparrow, E. M., Abraham, J. P., and Tong, J. C. K. "Archival correlations for average heat transfer coefficients for non-circular and circular cylinders and for spheres in cross-flow," *International Journal of Heat and Mass Transfer* Vol. 47, No. 24, 2004. pp. 5285-5296.**

[11]**Bragg, M. B., "A Similarity Analysis of the Droplet Trajectory Equations," AIAA 82-4285, AAIA Journal, Vol. 20, NO. 12, December 1982.**

[12]**Wright, W. B., "Users Manual for the NASA Glenn Ice Accretion Code LEWICE Version 3.0," available on the NASA LEWICE 3.0 release CD, April 2003.**

[13]**Bidwell, C.S., and Potapczuk, M.G., "Users Manual for the NASA Lewis Three-Dimensional Ice Accretion Code (LEWICE3D)," NASA TM 105974, 1993.**

Name	P_0	Velocity (m/s)	α (degrees)	γ (degrees)	Support	Grid
Pt06p5V085	6.5	85	0	0	No	Normal
Pt06p5V100	6.5	100	0	0	No	Normal
Pt06p5V135	6.5	135	0	0	No	Normal
Pt13p5V085	13.5	85	0	0	No	Normal
Pt13p5V100	13.5	100	0	0	No	Normal
Pt13p5V135	13.5	135	0	0	No	Normal
Attack5deg	13.5	85	5	0	No	Normal
Yaw5deg	13.5	85	0	5	No	Normal
Support	13.5	85	0	0	Yes	Normal
Pt13p5V085c	13.5	85	0	0	No	Coarsened
Pt13p5V085f	13.5	85	0	0	No	Refined

Table 1. Summary of cases (colors are used to highlight differences).

Name	Normalized Average Shroud Mass Flux
Pt06p5V085	0.7905
Pt06p5V100	0.7855
Pt06p5V135	0.7895
Pt13p5V085	0.7988
Pt13p5V100	0.7975
Pt13p5V135	0.7917
Attack5deg	0.7977
Yaw5deg	0.8045
Support	0.8034
Pt13p5V085c	0.8344
Pt13p5V085f	0.7871

Table 2. Average mass flux within shroud normalized by free stream mass flux.

Name	Re_{thick}	Scoop Front	Scoop Overall	Thick Front	Thick Overall
Pt06p5V085	3212	22.88	24.82	46.47	32.00
Pt06p5V100	3684	24.98	27.04	49.12	34.32
Pt06p5V135	4726	28.42	30.96	55.14	38.94
Pt13p5V085	6742	32.35	38.26	66.88	47.39
Pt13p5V100	7768	35.30	41.07	70.72	50.82
Pt13p5V135	9843	40.49	46.93	79.02	57.06
Pt13p5V085c	7043	27.46	33.31	67.98	43.63
Pt13p5V085f	6643	32.40	40.56	66.15	47.05

Table 3. Thick and Scoop average Nusselt numbers for straight on cases. (Thick and Scoop have the same diameter).

Name	Re_{thin}	Thin Front	Thin Overall
Pt06p5V085	813	22.97	15.24
Pt06p5V100	932	24.51	16.42
Pt06p5V135	1196	27.53	18.63
Pt13p5V085	1706	32.99	22.66
Pt13p5V100	1965	35.25	24.37
Pt13p5V135	2490	39.31	27.28
Pt13p5V085c	1782	33.83	21.67
Pt13p5V085f	1681	32.53	22.18

Table 4. Thin average Nusselt number for straight on cases.

Name	Re_{thick}	Scoop Front	Scoop Overall	Thick Front	Thick Overall
Pt13p5V085	6742	32.35	38.26	66.88	47.39
Attack5deg	6733	32.15	38.13	66.96	47.33
Yaw5deg	6790	32.11	37.69	67.18	47.53
Support	6781	32.04	37.02	66.87	47.48

Table 5. Thick and Scoop average Nusselt numbers for other cases. (Thick and Scoop have the same diameter).

Name	Re_{thin}	Thin Front	Thin Overall
Pt13p5V085	1706	32.99	22.66
Attack5deg	1703	32.86	22.56
Yaw5deg	1718	33.00	22.67
Support	1716	32.97	22.64

Table 6. Thin average Nusselt number for other cases.

Geometry	Total Pressure	Airspeed	Drop Size	Re_δ	K	K_0	$E_{m,2D}$	$E_{m,3D}$
	psia	m/s	Microns				Lewice2D	Lewice3D
Thin (021)	6.5	85	5	13.97	13.09	8.52	0.931	0.829
Thin (021)	6.5	85	20	55.87	209.38	92.45	0.990	0.957
Thin (021)	6.5	85	50	139.68	1308.63	408.18	0.995	0.989
Thin (021)	6.5	85	100	279.36	5234.52	1202.88	0.995	0.996
Thin (021)	13.5	85	5	29.01	13.09	7.09	0.923	0.820
Thin (021)	13.5	85	20	116.04	209.38	70.45	0.990	0.957
Thin (021)	13.5	85	50	290.11	1308.63	295.48	0.995	0.988
Thin (021)	13.5	85	100	580.21	5234.52	842.95	0.995	0.995
Thin (021)	13.5	135	5	42.97	20.78	10.00	0.943	0.841
Thin (021)	13.5	135	20	171.89	332.46	94.97	0.990	0.963
Thin (021)	13.5	135	50	429.73	2077.86	388.69	0.995	0.990
Thin (021)	13.5	135	100	859.47	8311.45	1092.38	0.995	0.996
Thick (083)	6.5	85	5	13.97	3.31	2.16	0.782	0.655
Thick (083)	6.5	85	20	55.87	52.97	23.39	0.974	0.936
Thick (083)	6.5	85	50	139.68	331.04	103.26	0.992	0.985
Thick (083)	6.5	85	100	279.36	1324.16	304.29	0.996	0.995
Thick (083)	13.5	85	5	29.01	3.31	1.79	0.754	0.627
Thick (083)	13.5	85	20	116.04	52.97	17.82	0.968	0.926
Thick (083)	13.5	85	50	290.11	331.04	74.75	0.990	0.981
Thick (083)	13.5	85	100	580.21	1324.16	213.24	0.995	0.993
Thick (083)	13.5	135	5	42.97	5.26	2.53	0.816	0.686
Thick (083)	13.5	135	20	171.89	84.10	24.03	0.975	0.942
Thick (083)	13.5	135	50	429.73	525.63	98.33	0.992	0.985
Thick (083)	13.5	135	100	859.47	2102.52	276.34	0.995	0.994
Half-Pipe	6.5	85	5	13.97	3.31	2.16	0.892	0.727
Half-Pipe	6.5	85	20	55.87	52.97	23.39	0.983	0.943
Half-Pipe	6.5	85	50	139.68	331.04	103.26	0.992	0.986
Half-Pipe	6.5	85	100	279.36	1324.16	304.29	0.994	0.996
Half-Pipe	13.5	85	5	29.01	3.31	1.79	0.854	0.703
Half-Pipe	13.5	85	20	116.04	52.97	17.82	0.979	0.935
Half-Pipe	13.5	85	50	290.11	331.04	74.75	0.991	0.983
Half-Pipe	13.5	85	100	580.21	1324.16	213.24	0.994	0.994
Half-Pipe	13.5	135	5	42.97	5.26	2.53	0.892	0.757
Half-Pipe	13.5	135	20	171.89	84.10	24.03	0.983	0.949
Half-Pipe	13.5	135	50	429.73	525.63	98.33	0.992	0.987
Half-Pipe	13.5	135	100	859.47	2102.52	276.34	0.994	0.995

Table 7. Total collection efficiency results for straight on cases without support.

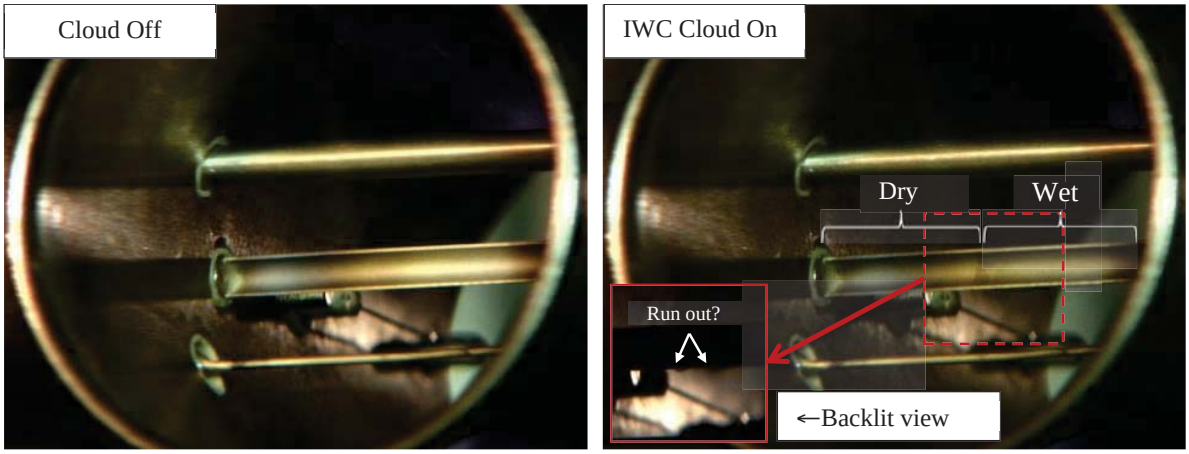

Figure 1. Images of the front face of the SEA multi-wire probe taken during a test where the ice water content was nominally 6 g/m³ and the freestream velocity was 85 m/s, total pressure was 93 kPa, and the total air temperature was -1 ℃. With the ice cloud on, the half-pipe of the SEA multi-wire probe has what appear to be dry and wetted regions. The inset view shows an image of the probe during the same data point but backlit producing a shadow view of the elements.

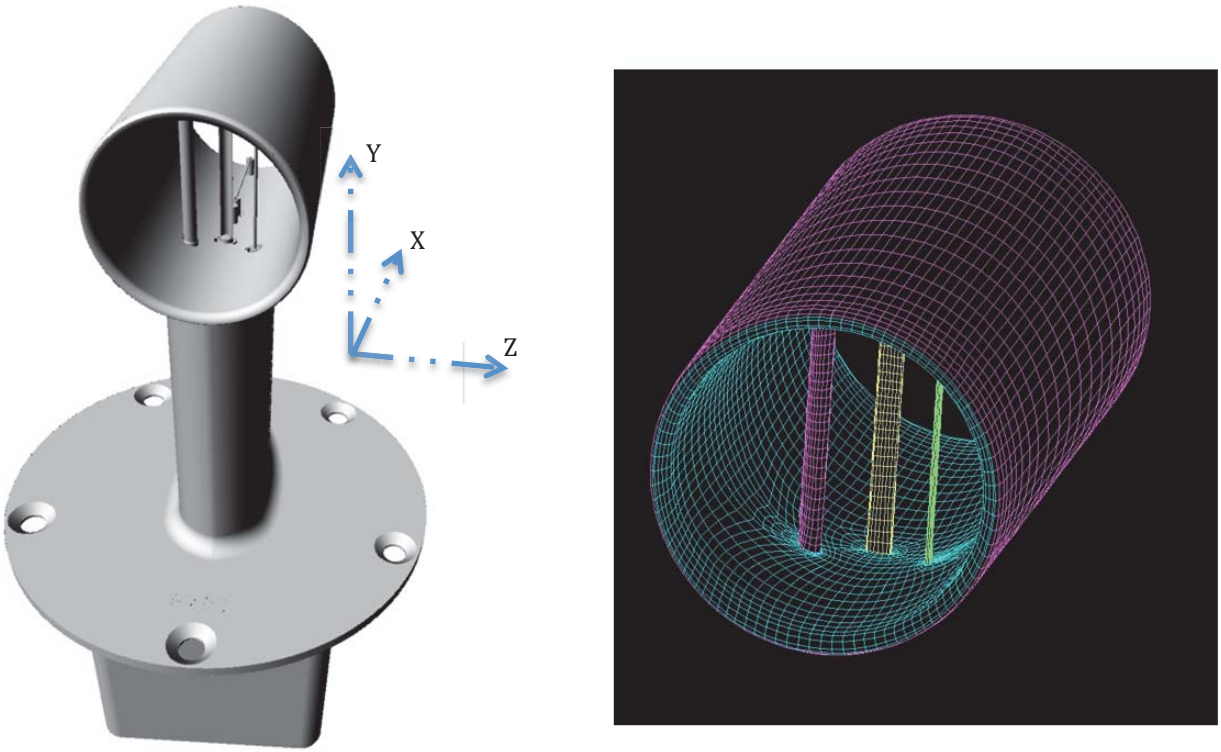

Figure 2. CAD representation (left) and surface mesh for CFD simulation. Angle of attack refers to a rotation about the Y-axis. Yaw refers to a rotation about the Z-axis.

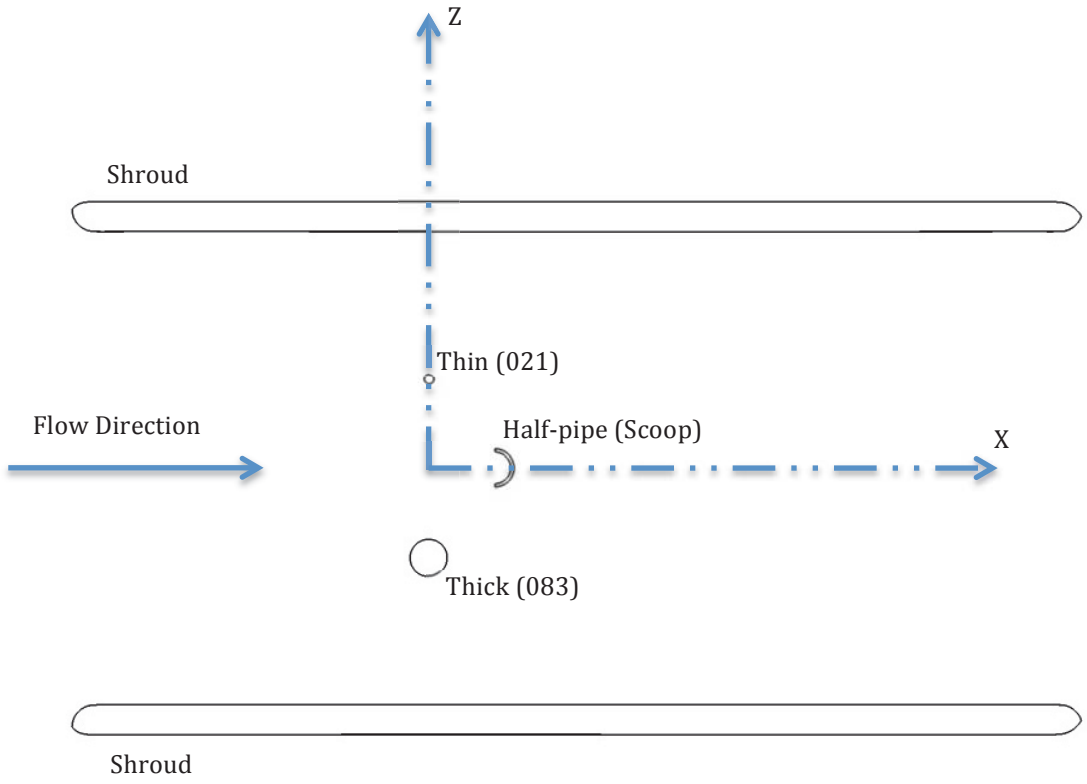

Figure 3. Schematic showing coordinate system.

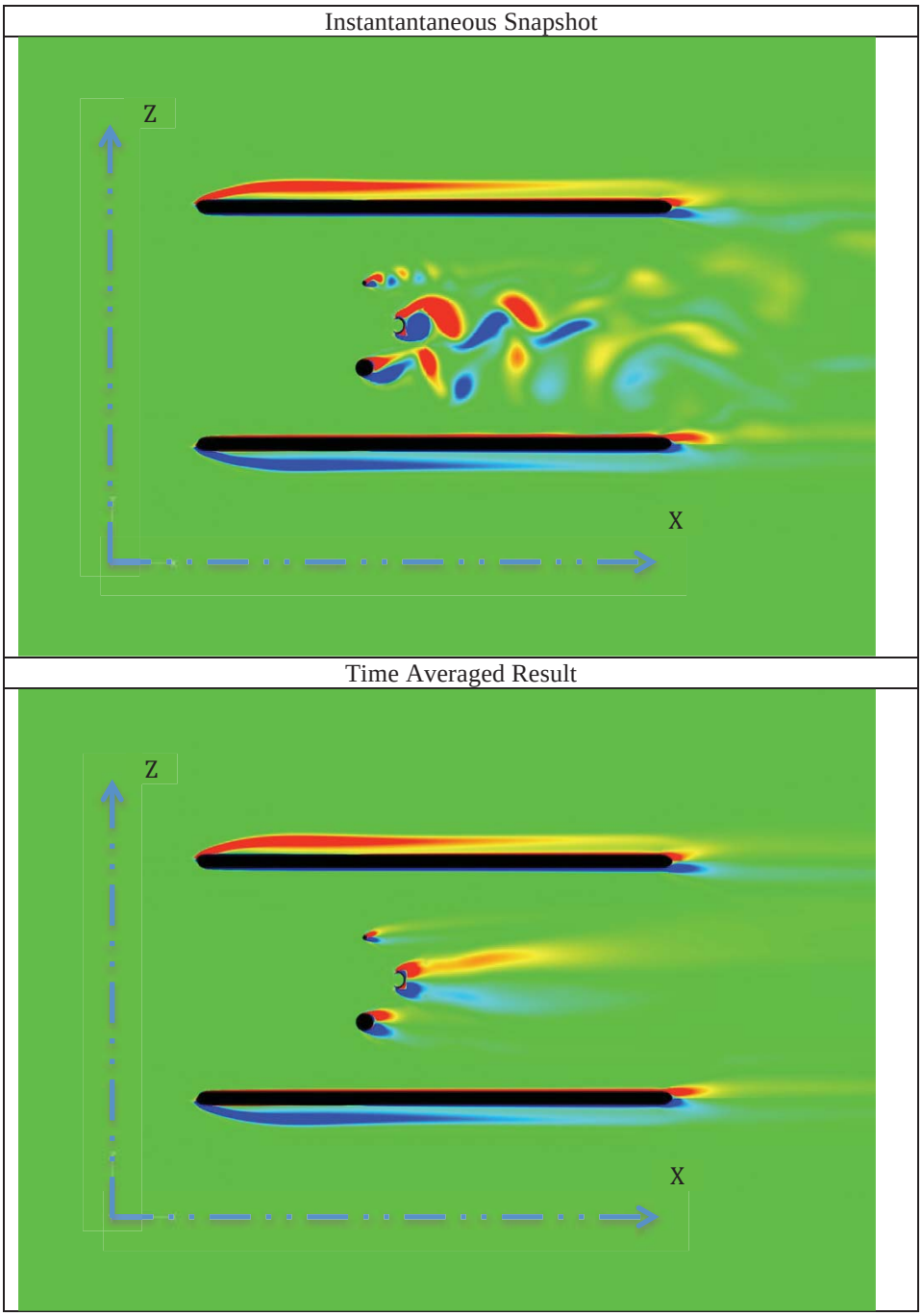

Figure 4. Comparison of y-vorticity for instantaneous versus time averaged result. Red is positive and blue is negative.

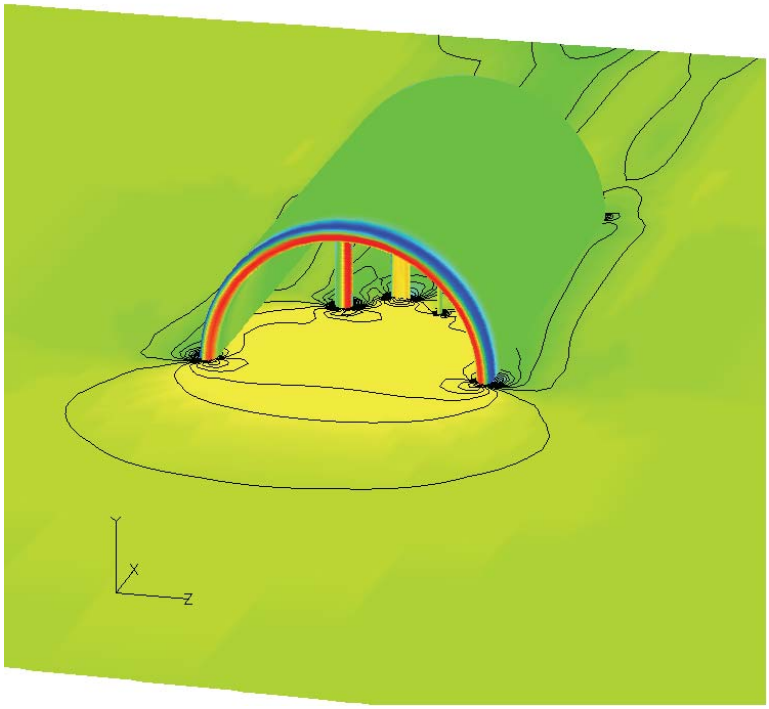

Figure 5. Pressure in symmetry plane and on surfaces.

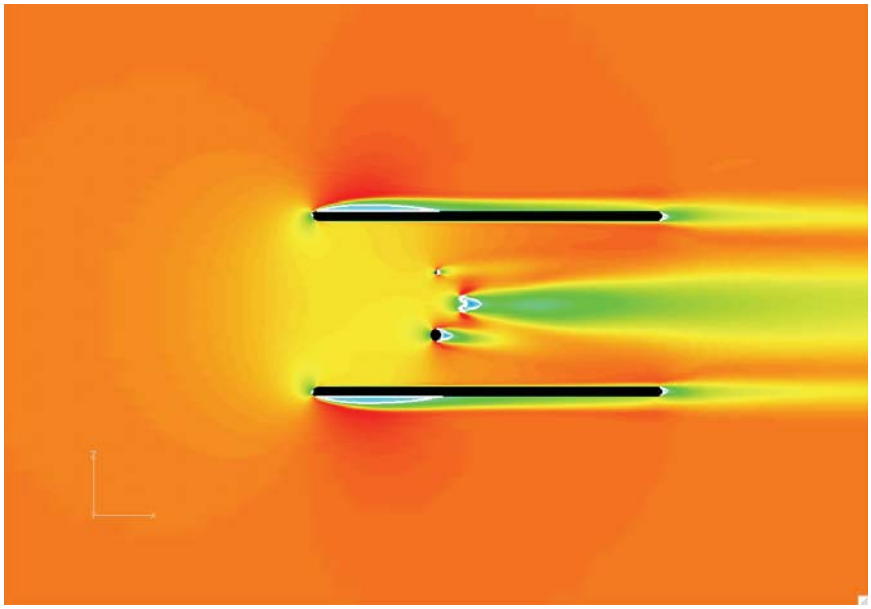

Figure 6. Axial velocity in the symmetry plane. White lines, representing zero velocity, enclose reverse flow regions.

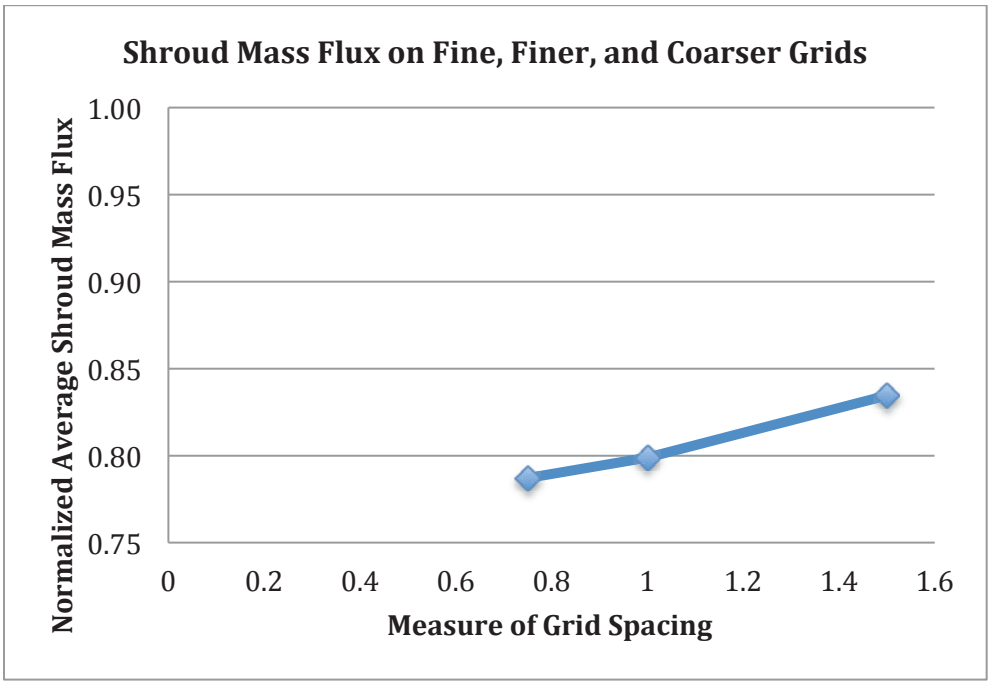

Figure 7. Normailized average shroud mass flux versus grid spacing for case Pt13p5_V085. (i.e. the mass flow through the shroud divided by the freestream mass flow through the same cross sectional area)

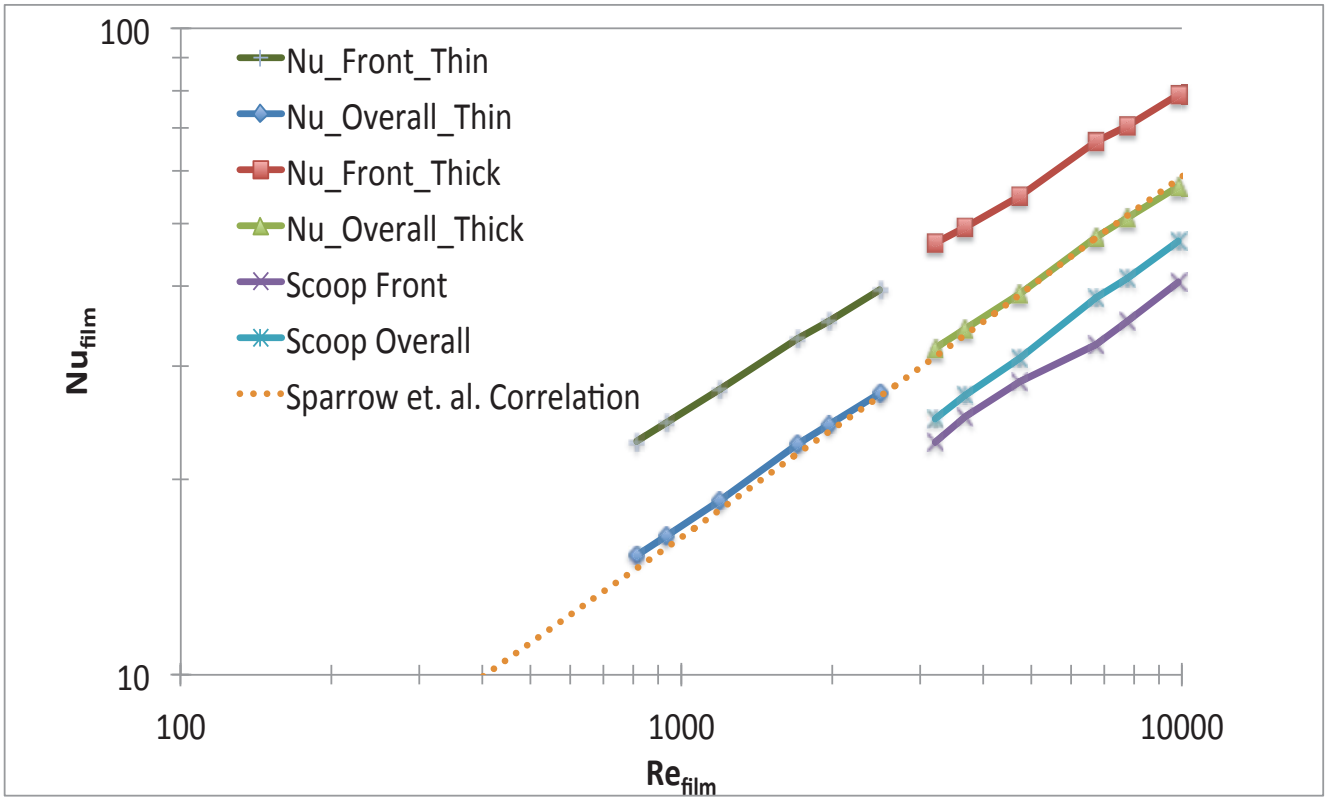

Figure 8. Nusselt number results for straight on cases.

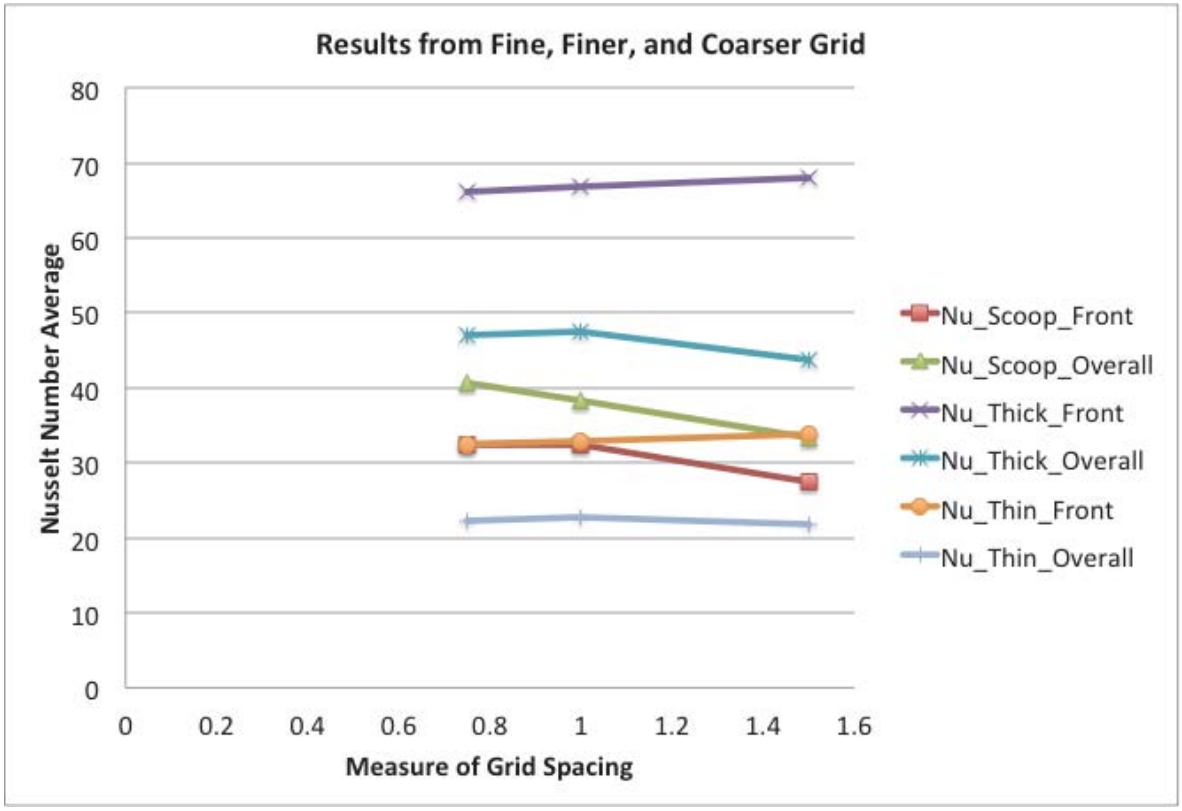

Figure 9. Nusselt number averages versus grid spacing for case Pt13p5_V085.

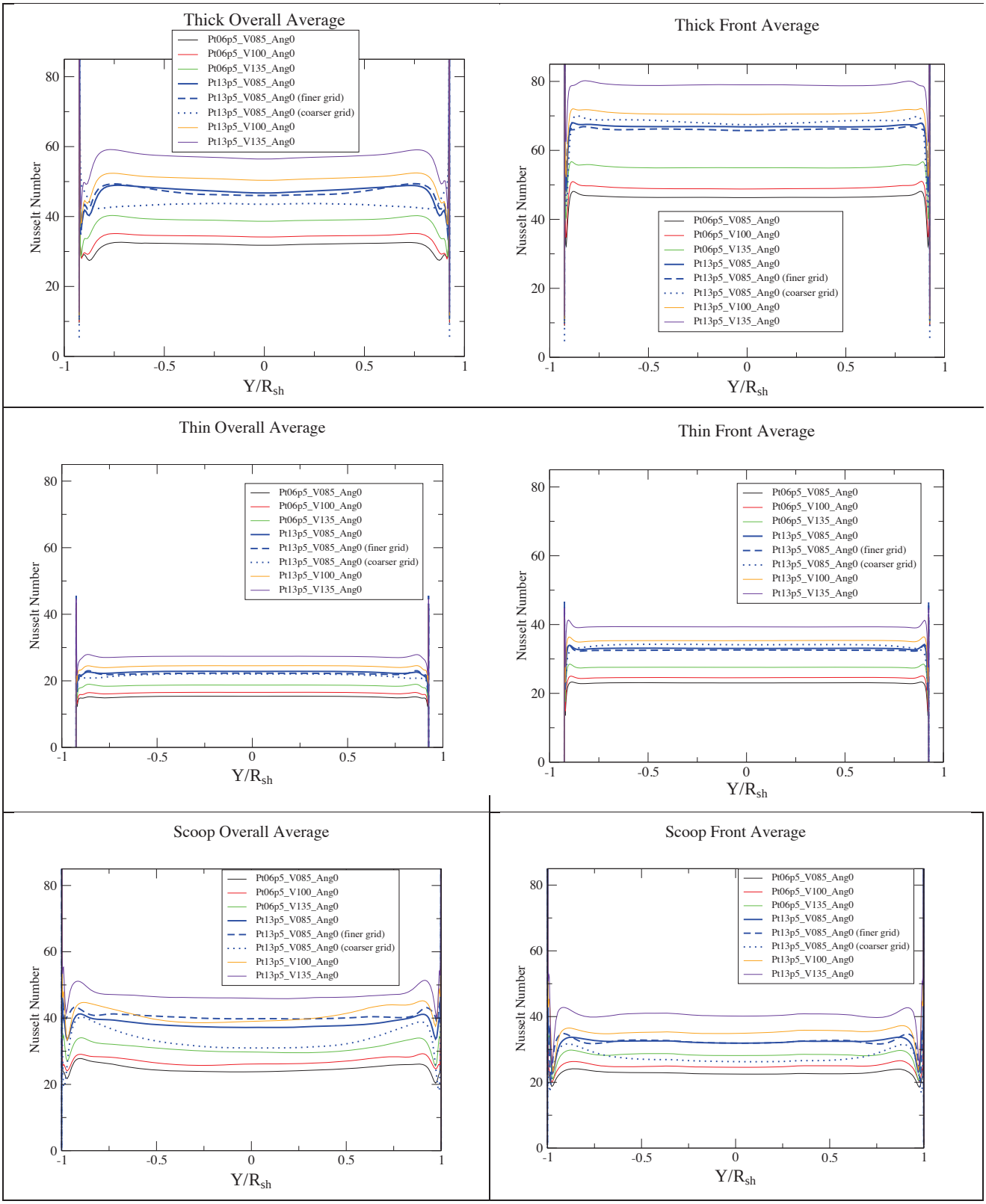

Figure 10. Spanwise variation of average Nusselt numbers for straight on cases.

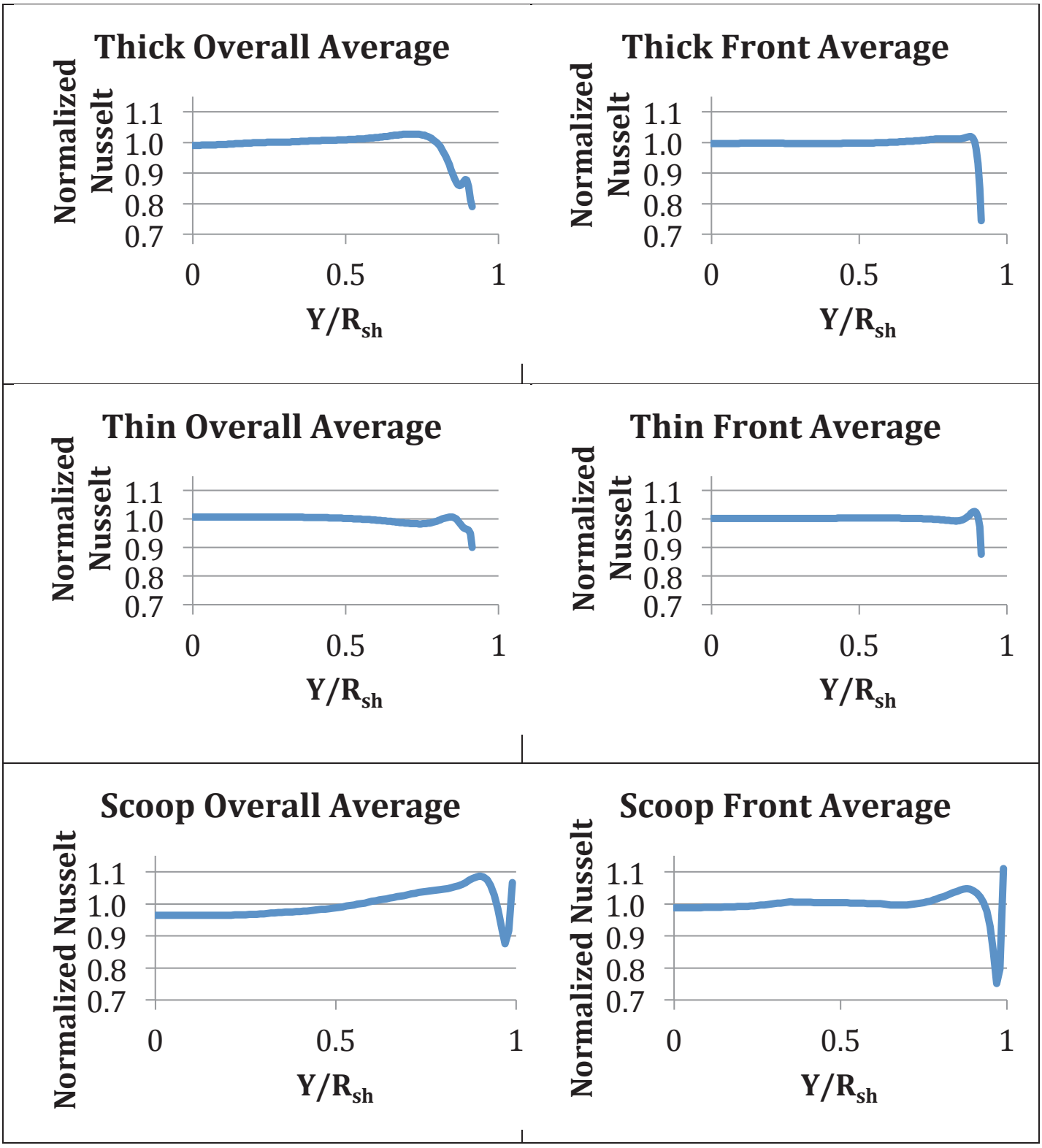

Figure 11. Normalized Nusselt number averaged from all six straight on cases.

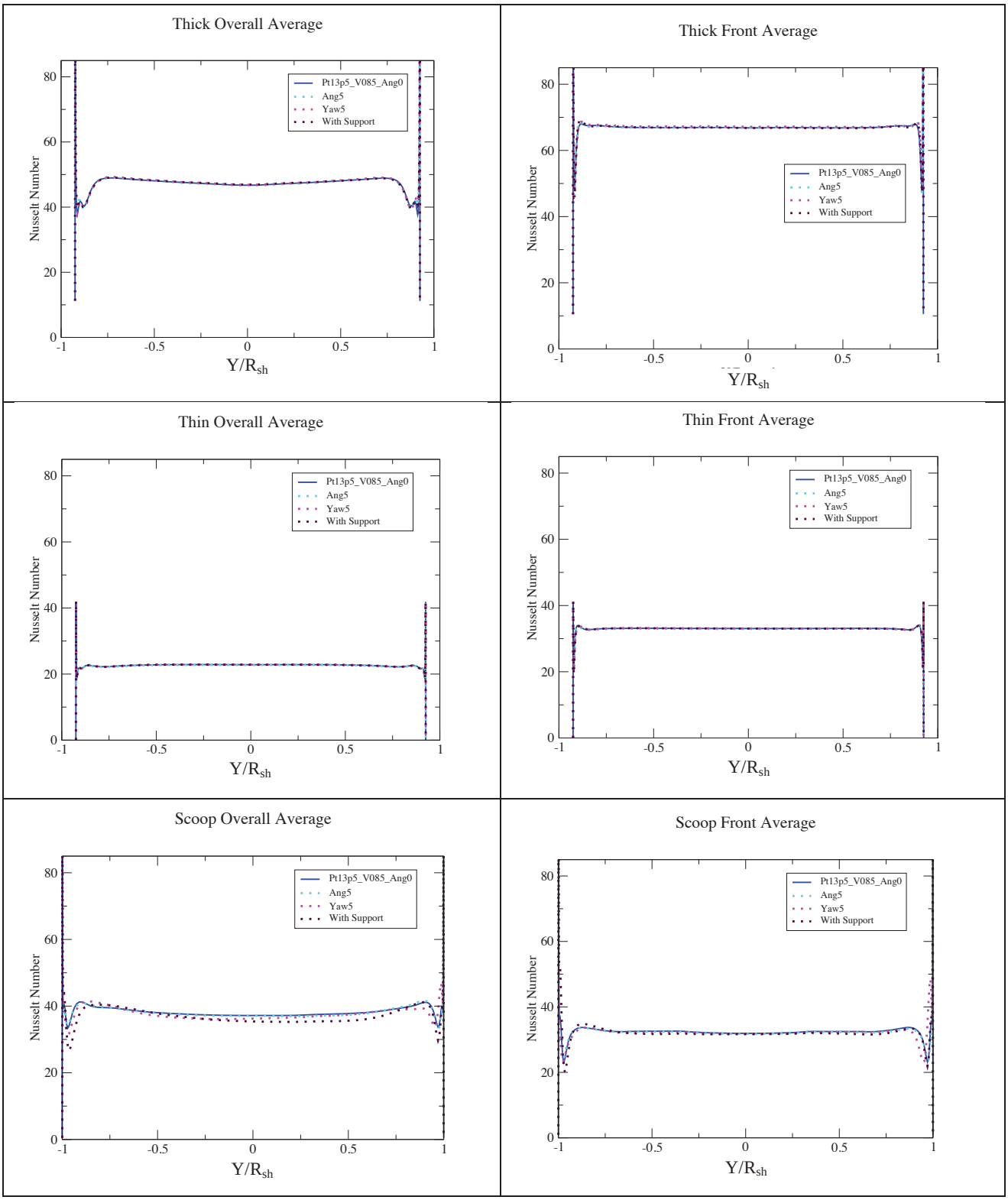

Figure 12. Average Nusselt numbers for Angle of attack, Yaw, and Support cases, compared to straight on at same conditions

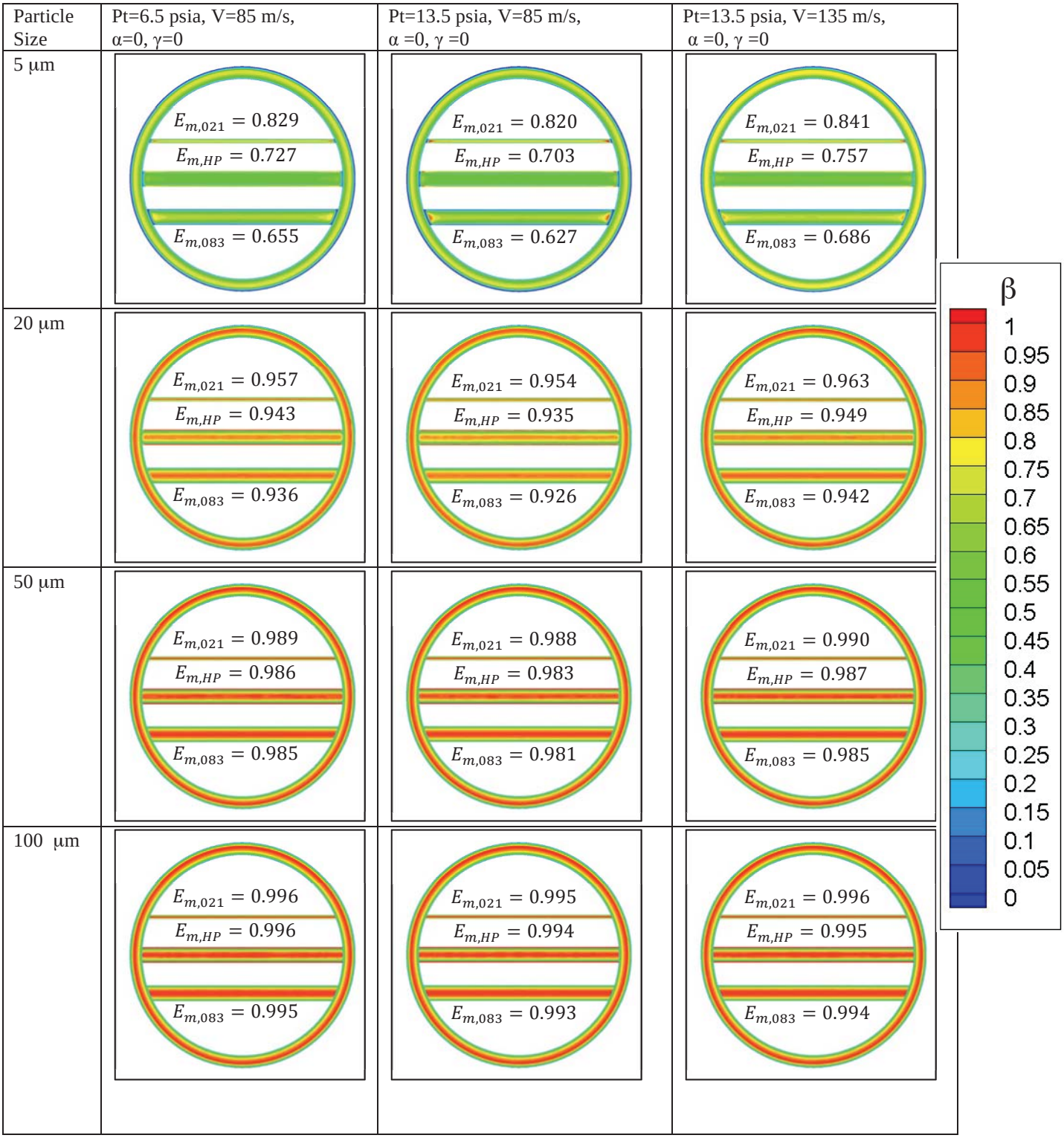

Figure 13. Local collection efficiency for several particle sizes (straight on cases). Value of total collection efficiency for each heated element is also included to quantify fraction of particles captured by each element.

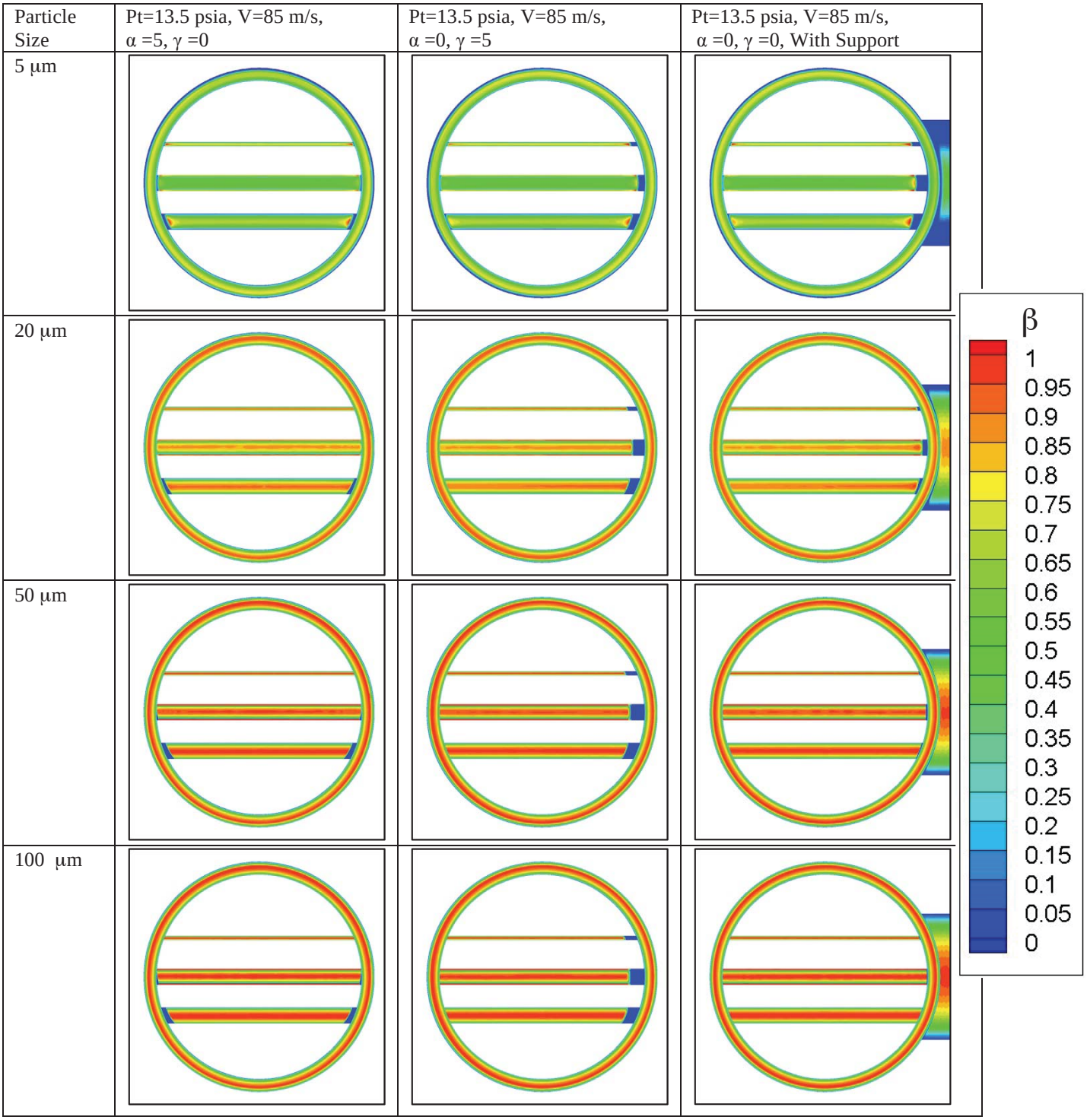

Figure 14. Collection efficiency for several particle sizes (angle of attack, yaw and support cases).

Particle Size	Pt=6.5 psia, V=85 m/s, α =0, γ =0	Pt=13.5 psia, V=85 m/s, α =0, γ =0	Pt=13.5 psia, V=135 m/s, α =0, γ =0
100 μm	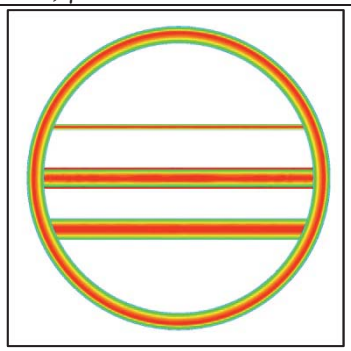	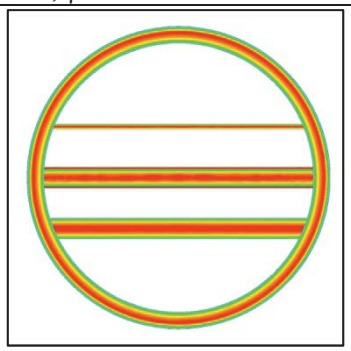	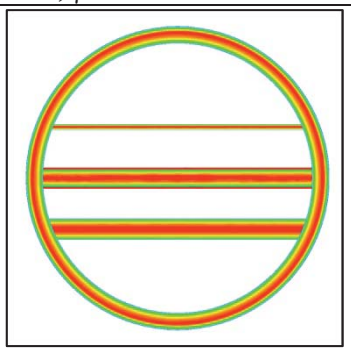
100 μm Splashing	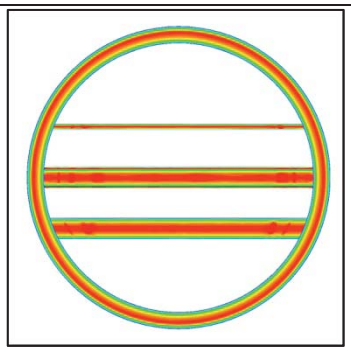	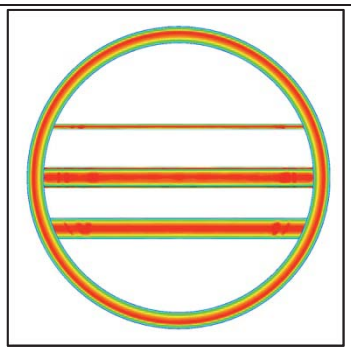	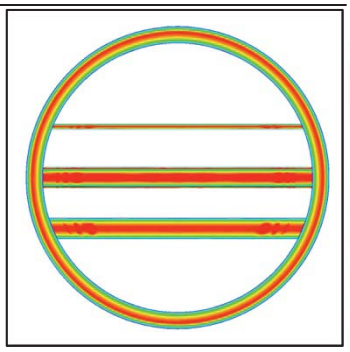

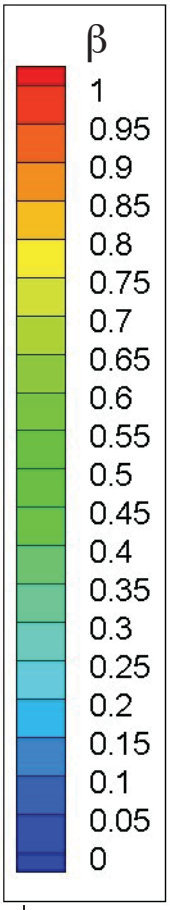

Figure 15. Collection efficiency. Splashing compared to no splashing (straight on cases).

Particle Size	Pt=13.5 psia, V=85 m/s, α =5, γ =0	Pt=13.5 psia, V=85 m/s, α =0, γ =5	Pt=13.5 psia, V=85 m/s, α =0, γ =0, With Support
100 μm	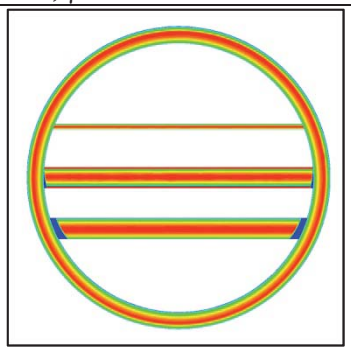	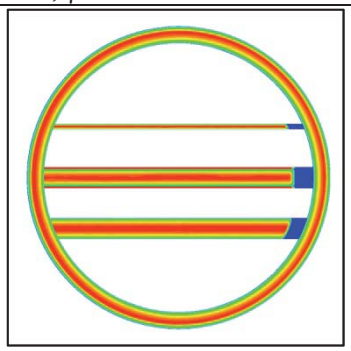	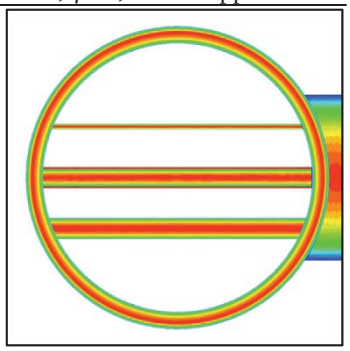
100 μm Splashing	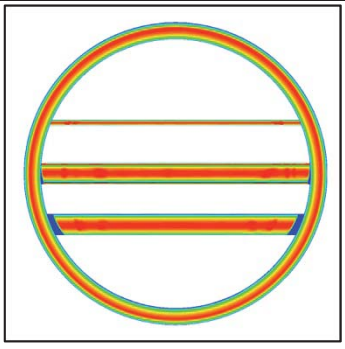	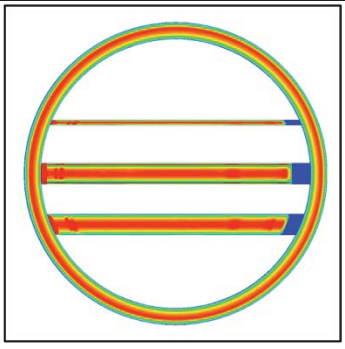	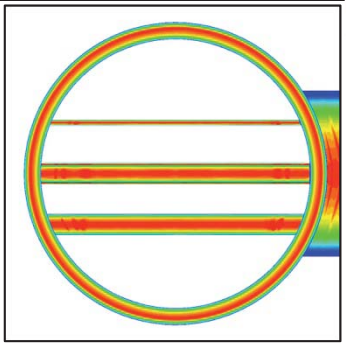

Figure 16. Collection efficiency. Splashing compared to no splashing (angle of attack, yaw, and support cases.